SCIENCE CHINA
Chemistry

•ARTICLES•

May 2022 Vol.65 No.5: 934–942
https://doi.org/10.1007/s11426-022-1221-4

An *in-situ* generated composite solid-state electrolyte towards high-voltage lithium metal batteries

Qinglei Wang[1,3†], Tiantian Dong[1,2†], Qian Zhou[1], Zili Cui[1], Xuehui Shangguan[3], Chenglong Lu[1], Zhaolin Lv[1], Kai Chen[1], Lang Huang[1], Huanrui Zhang[1*] & Guanglei Cui[1*]

[1]*Qingdao Industrial Energy Storage Research Institute, Qingdao Institute of Bioenergy and Bioprocess Technology, Chinese Academy of Sciences, Qingdao 266100, China;*
[2]*School of Materials Science and Engineering, Ocean University of China, Qingdao 266042, China;*
[3]*School of Materials Science and Engineering, Linyi University, Linyi 276000, China*

Received January 18, 2022; accepted March 3, 2022; published online April 7, 2022

The solid-state electrolyte (SSE) has promising applications in next-generation lithium (Li) metal batteries (LMBs) because of its significantly enhanced safety and more compatible interface characteristics than flammable traditional liquid electrolytes. However, only a few attempts have achieved high-performance high-voltage LMBs, which is attributed to the fact that both high ionic conductivity and good compatibility with electrodes can hardly be achieved simultaneously. Herein, a composite solid-state electrolyte (CSE) based on star-shaped siloxane-based polymer electrolyte coupled with $Li_{6.75}La_3Zr_{1.75}Ta_{0.25}O_{12}$ (LLZTO) ceramic fillers is designed and prepared through a facile *in-situ* polymerization method. The obtained CSE exhibits high ionic conductivity (*i.e.*, 1.68×10^{-4} S cm^{-1} at a temperature of 60 °C), superior anodic stability, and high Li-ion transference number (*i.e.*, 0.53) because of the multifunctional synergistic effect of the polymer electrolyte with LLZTO ceramic fillers. Moreover, the as-developed CSE shows excellent compatibility with Li anodes. As a result, the as-developed CSE enables the development of long-life 4.4-V-class solid-state LMBs with a $LiCoO_2$ cathode, with 79.7% capacity retention and 99.74% average Coulombic efficiency after 500 cycles at a 0.5 C rate. Postmortem analysis of cycled batteries confirms that such superior battery performance can be mainly ascribed to the formation of a compatible electrode/electrolyte interface. Furthermore, excellent safety features can be observed in $LiCoO_2$/Li pouch batteries. This work provides an important guide for the rational design of SSEs for high-voltage LMBs.

composite solid-state electrolyte, *in-situ*, lithium metal batteries, high-voltage

Citation: Wang Q, Dong T, Zhou Q, Cui Z, Shangguan X, Lu C, Lv Z, Chen K, Huang L, Zhang H, Cui G. An *in-situ* generated composite solid-state electrolyte towards high-voltage lithium metal batteries. *Sci China Chem*, 2022, 65: 934–942, https://doi.org/10.1007/s11426-022-1221-4

1 Introduction

Lithium metal batteries (LMBs) have been regarded as the "holy grail" of next-generation high-energy storage systems because of their ultrahigh theoretical specific capacity (*i.e.*, 3,860 mAh g^{-1} or 2,061 mAh cm^{-3}) and ultralow redox potential (−3.04 V *vs*. standard hydrogen electrode) of Li metal anodes [1–3]. However, the use of traditional liquid electrolytes, which easily leak and are highly flammable, leads to safety hazards, posing a significant challenge to their commercial applications. As a good candidate for conventional liquid electrolytes, solid-state electrolytes (SSEs) have attracted ever-increasing attention because they are expected to fundamentally eliminate the safety issues of commercially available LMBs [4].

In general, SSEs can be mainly classified into three categories: inorganic solid-state electrolytes (ISEs), solid-state

†These authors contributed equally to this work.
*Corresponding authors (email: cuigl@qibebt.ac.cn; zhanghr@qibebt.ac.cn)

polymer electrolytes (SPEs), and composite solid-state electrolytes (CSEs). ISEs exhibit optimum ionic conductivity, nearly unity Li-ion transference number, high electrochemical oxidation resistance, and superior mechanical strength; however, large solid-solid interface impedance between electrodes and ISEs restricts their practical application [5]. Moreover, the large-scale preparation of a thin, dense solid film <100 μm is difficult. Compared with ISEs, SPEs possess non-negligible advantages, such as excellent shape versatility and flexibility, low-cost processability, and improved interfacial compatibility. However, SPEs suffer from low ambient-temperature conductivity ($<10^{-3}$ S cm^{-1}) and poor anodic stability (<4 V) [6]. Combining the strengths of ISEs and SPEs, CSEs are practically more viable for commercial applications [7]. Thus far, various strategies have been employed to fabricate CSEs, such as employing ceramic nanoparticles/nanowires [8], aligned or hierarchical configuration design [9], three-dimensional (3D) nanostructured framework [10], and surface wetting of ceramic fillers with polymers [11].

Despite some progress, to our knowledge, only a few efforts have achieved high-voltage (>4.3 V *vs*. Li/Li$^+$) LMBs with distinguished comprehensive performance, which is attributed to the fact that CSEs with both high ionic conductivity and good compatibility with electrodes are difficult to obtain. Furthermore, the relatively tedious fabrication process, such as the *ex-situ* solution casting technique accompanied by the use of noxious organic solvents, can hardly meet the practical needs of large-scale commercial production.

Recently, siloxane-based polymer electrolytes have been attracting considerable attention because of their high thermal and chemical stabilities, flexible Si–O–Si backbones, and nontoxicity [12]. In particular, a previous study reported that organosilicon can help construct a uniform solid cathode electrolyte interphase (CEI) film [13]. Moreover, a star-shaped or hyperbranched polymer matrix design is preferable owing to the enhanced ionic conductivity and electrochemical performance compared with linear polymers [14]. Notably, compared with traditional *ex-situ* solution casting methods, the *in-situ* technique is considered to be a more facile strategy for low-cost and large-scale fabrication [15]. For instance, Zhou *et al*. [16] developed a hierarchical multifunctional SPE with near-single ion conduction *via in-situ* polymerization, enabling stable cycling of solid-state Li-ion cells. Archer *et al*. [17] fabricated an SPE *via in-situ* ring-opening polymerization, which enables fast interfacial transport for secondary Li batteries. Recently, our group has designed 3D inorganic porous CSE coupled with *in-situ*-polymerized poly(ethylene glycol) methyl ether acrylate (PDEM), which enables the construction of a fast ion channel and stable electrolyte/electrode interface [18,19]. However, the comprehensive performance, particularly the high-voltage cycling performance, of the aforementioned system needs further improvement. To the best of our knowledge, only a few works have been devoted to siloxane-based CSE. Inspired and encouraged by the aforementioned work, we anticipate that the *in-situ* generated composite electrolyte based on star-shaped siloxane-based electrolytes coupled with ceramic fillers will exhibit superior comprehensive performance.

Herein, we develop a novel CSE P(PDEM-D4)-CSE comprising a star-shaped siloxane-based SPE coupled with $Li_{6.75}La_3Zr_{1.75}Ta_{0.25}O_{12}$ (LLZTO) ceramic filler. P(PDEM-D4)-CSE was prepared by the facile *in-situ* preparation method, which endowed it with close interface contact. The as-designed electrolyte exhibits a high thermal decomposition temperature and excellent thermal dimensional stability. Moreover, because of the synergy between P(PDEM-D4)-PE and LLZTO, the as-developed CSE shows a high ionic conductivity, high Li-ion transference number, and wide electrochemical stability window. It is worth noting that the as-developed CSE enables homogeneous Li deposition. Resultantly, the 4.4 V $LiCoO_2$/Li battery with the as-developed CSE presents excellent cycling stability and rate capability at a temperature of 60 °C. Postmortem analysis of cycled LMBs reveals that such superior electrochemical performance can be mainly ascribed to the formation of a compatible electrode/electrolyte interface. Furthermore, the as-assembled pouch cells present outstanding safety characteristics under harsh conditions.

2 Experimental

The experimental details can be found in the Supporting Information online.

3 Results and discussion

3.1 Preparation and characterization of the as-developed CSE

P(PDEM-D4)-CSE was prepared *via* facile *in-situ* radical polymerization of the electrolyte precursor solution containing the monomer 2,4,6,8-tetramethyl-2,4,6,8-tetravinylcyclotetrasiloxane (D4), PDEM, lithium difluoro (oxalate)borate (LiDFOB), and LLZTO particles (Figure 1a, experimental section in the Supporting Information online). Among them, D4, as a part of the polymer backbone, can effectively increase the free volume for the segmental motions of polymer chains, thereby enhancing ionic conductivity. PDEM, as a Li$^+$ carrier, provides channels for Li-ion transport. LiDFOB, as the Li source, supplies Li$^+$ and DFOB$^-$ and participates in the construction of the interface film. LLZTO, as an active ceramic filler, not only enhances

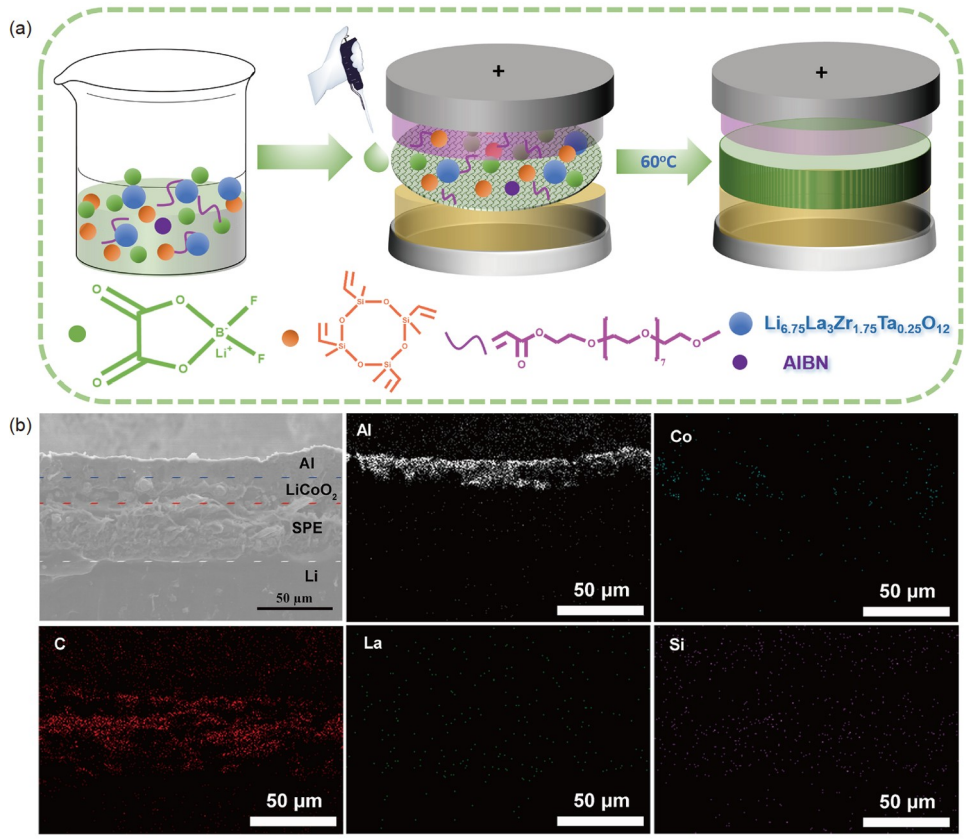

Figure 1 (a) Schematic illustration of the *in situ* preparation route of CSE; (b) typical cross-sectional SEM images of the $LiCoO_2$/CSE/Li battery and its corresponding energy-dispersive X-ray spectroscopy (color online).

the segmental motion of the polymer matrix by reducing crystallinity and increasing the free volume of the polymer matrix, which helps construct more channels for ion transport, but also acts as the anionic receptor that promotes the dissociation of Li salts and the increase of free Li-ion concentration. Moreover, the percolation behavior resulting from the adsorption effect at the second-phase interface can help enhance ionic conductivity. Benefiting from the *in-situ* polymerization strategy, the electrolyte precursor solutions exhibit moderate viscosity and good wetting of the lithium cobalt oxide ($LiCoO_2$) cathode (Table S1 and Figure S3, Supporting Information online), which enables the construction of an efficient ion transport network within electrodes. Fourier transform infrared spectroscopy analysis and the digital images before and after polymerization indicate that

P(PDEM-D4)-CSE was successfully obtained (Figures S4 and S5). The as-developed CSE delivers a thickness of 35 μm and exhibits close contact with the electrodes, as evidenced by the typical cross-sectional scanning electron microscopy (SEM) images (Figure 1b). Furthermore, the energy-dispersive X-ray spectroscopy mapping analysis reveals the homogeneous distribution of elements in the CSE (see Figure 1b and Figure S6), which helps construct a fast ion transport network.

As shown in Figure S7a, the polymer matrix in P(PDEM-D4)-CSE, as well the corresponding polymer electrolyte without LLZTO and the one without both LLZTO and D4 (hereafter denoted as P(PDEM-D4)-PE and P(PDEM)-PE, respectively), has an amorphous phase, which is beneficial to Li-ion transport. The diffraction peaks of LiDFOB are absent in all of the SSEs, indicating the absence of salt particles in the electrolyte. Moreover, no new crystallization peaks appear in P(PDEM-D4)-CSE compared with LLZTO, indicating good chemical compatibility between LLZTO and P(PDEM-D4)-PE.

Differential scanning calorimetry measurement indicates that P(PDEM-D4)-CSE shows an amorphous structure with a glass transition temperature (T_g) of −46 °C, which is lower than that of the traditional polyethylene oxide (PEO) counterpart (−30 °C; Figure S7b). The decreased T_g indicates that the as-developed CSE possess fast segmental motions of polymer chains and low activation energy (E_a) for ion transport. As presented in thermogravimetric curves (Figure S7c), P(PDEM-D4)-CSE shows a thermal decomposition temperature of approximately 300 °C. Apart from this, P(PDEM-D4)-CSE can be hardly ignited, in stark contrast to the highly combustible traditional liquid electrolyte (*i.e.*, 1 M $LiPF_6$-diethyl carbonate/ethyl methyl carbonate/dimethyl carbonate; Video S1 and Figure S7d, Supporting Information

online). P(PDEM-D4)-CSE can also achieve thermal dimensional stability that is superior to that of a commercial polypropylene separator (shrinkage rate of 1% *vs*. 45%; Figure S7e). The superior thermal decomposition temperature and thermal dimensional stability of the as-developed CSE help achieve outstanding safety characteristics for LMBs. Moreover, a tensile strength of 1.16 MPa and an elongation at break of approximately 7% at room temperature are obtained for P(PDEM-D4)-CSE films (Figure S7f), indicating their promising applications in roll-to-roll LMB assembly processing.

The ion-conductive behavior of the as-developed CSE as a function of the temperature and role of the component is investigated (Figure 2a, b and Tables S2–S5). Meanwhile, the corresponding E_a for ion transport is obtained through Vogel-Tammann-Fulcher fitting. The molar ratio of ethylene oxide/Li salt is set to 20, which is reported to result in high ionic conductivity [20,21]. Notably, ionic conductivity increases with the increase of temperature mainly because of the fast segmental motion of the polymer matrix (Figure 2a, b). For P(PDEM-D4)-PE, ionic conductivity first increases and then decreases with the increase of the content of D4, and SPE with 2wt% D4 exhibits the highest conductivities at different temperatures (Figure 2a and Table S2). This result can be ascribed to the fact that the presence of relatively less D4 improves the ion transport kinetics (Table S3) because of the low T_g of D4 motifs, whereas more D4 (>2 wt%) decreases the free volume for the segmental motions of polymer chains originating from the increased polymeric crosslinking degree. By setting the weight ratio of D4 to 2 wt %, a similar ionic conductivity tendency with the increase of the content of LLZTO is observed, and 5 wt% LLZTO helps achieve the optimum ion transport kinetics (Figure 2b and Tables S4 and S5). P(PDEM-D4)-CSE with

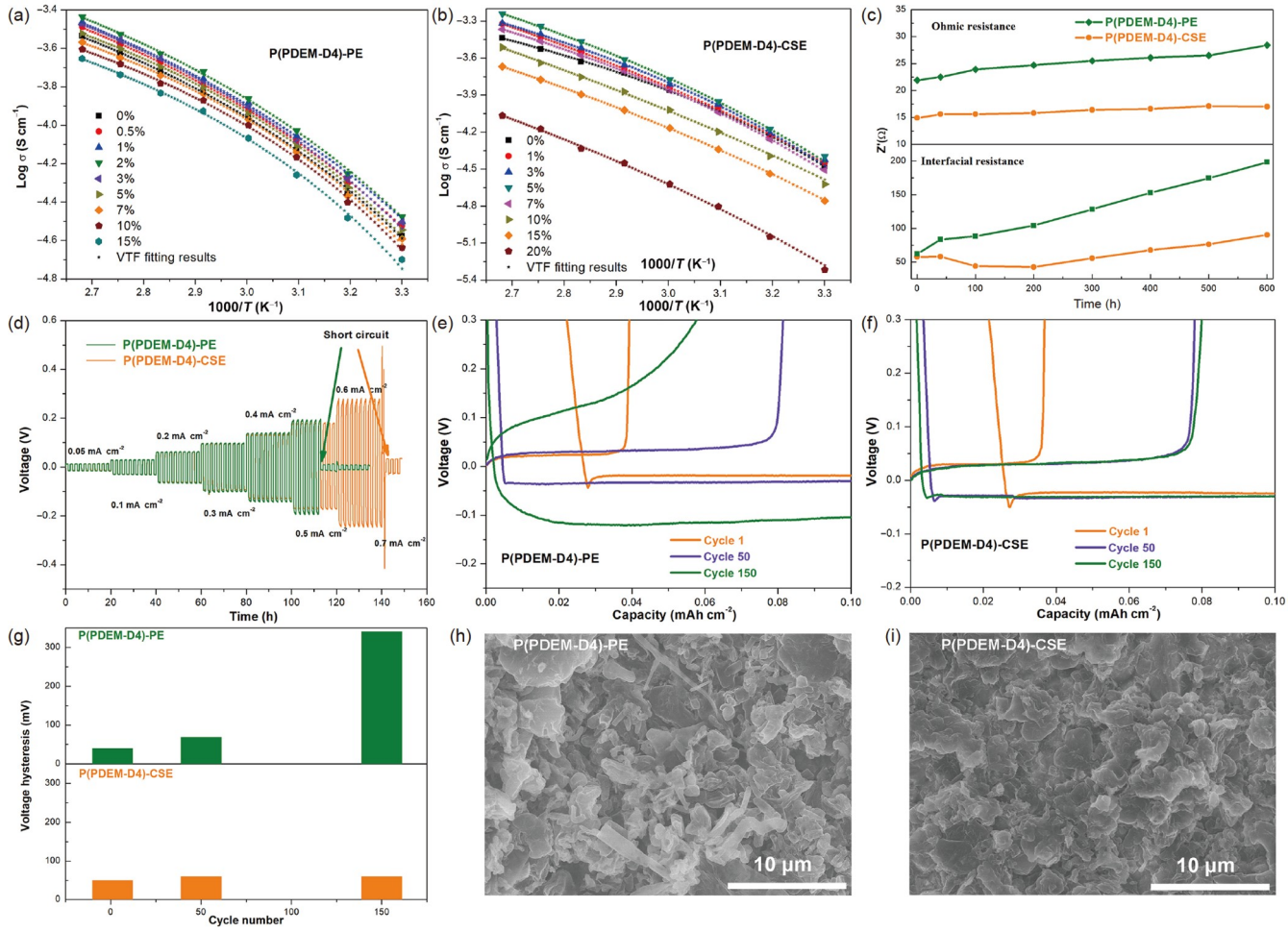

Figure 2 Ionic conductivities of P(PDEM-D4)-PE (a) and P(PDEM-D4)-CSE (b) as a function of the weight percentages of D4 and LLZTO at different temperatures; (c) evolution of the ohmic and interfacial resistance of Li/Li symmetric cells with P(PDEM-D4)-PE and P(PDEM-D4)-CSE after varied cycling times at a temperature of 60 °C; (d) Li plating/stripping of Li/Li symmetric cells with P(PDEM-D4)-PE or P(PDEM-D4)-CSE at current densities of 0.05, 0.1, 0.2, 0.3, 0.4, 0.5, 0.6, and 0.7 mA cm^{-2} (1 h in each half cycle) and a temperature of 60 °C; Charge-discharge curves of Cu/(PDEM-D4)-PE/Li (e) and Cu/P(PDEM-D4)-CSE/Li (f) cells at a current density of 0.1 mA cm^{-2} (a deposition capacity of 0.1 mAh cm^{-2}) and a temperature of 60 °C; (g) the corresponding voltage hysteresis at varied cycles; (h, i) typical SEM images of Li metal plating on a Cu substrate after 150 cycles in the presence of P(PDEM-D4)-PE or P(PDEM-D4)-CSE (color online).

5 wt% LLZTO yields the optimum ionic conductivity (*i.e.*, 4.0×10^{-5}, 1.68×10^{-4}, and 5.73×10^{-4} S cm^{-1} at 30, 60, and 100 °C, respectively). This phenomenon can be attributed to the following reasons: (1) less LLZTO can be well dispersed within the as-developed CSE, which can not only enhance the segmental motion of the polymer matrix and construct more channels for ion transport but also act as the anionic receptor that promotes the dissociation of Li salts and increases the free Li-ion concentration [22]. Moreover, the percolation behavior resulting from the adsorption effect at the second-phase interface can help enhance ionic conductivity, as reported by Bae *et al*. [10]. (2) However, excess LLZTO (>5 wt%) easily leads to nanoparticle agglomeration, as a result of which the ionic conductivity decreases. Based on the aforementioned investigations, P(PDEM-D4)-CSE with 2 wt% D4 and 5 wt% LLZTO yields the optimum ionic conductivity (*i.e.*, 4.0×10^{-5}, 1.68×10^{-4}, and 5.73×10^{-4} S cm^{-1} at 30, 60 and 100 °C, respectively) and the lowest E_a (Tables S4 and S5); thus, it is chosen as the model for subsequent research. The fast ion transport of P(PDEM-D4)-CSE mainly results from the synergy between P(PDEM-D4)-PE and LLZTO.

As shown in Figure S8 and Table S6, P(PDEM-D4)-CSE shows a Li-ion transference number (t_{Li^+}) of 0.53, which is higher than those of P(PDEM)-PE and P(PDEM-D4)-CSE (*i.e.*, 0.31 and 0.39, respectively). The high t_{Li^+} of P(PDEM-D4)-CSE is ascribed to the synergy between P(PDEM-D4)-PE and LLZTO: (1) The use of D4 enhances the segmental motions of polymer chains, thereby facilitating fast Li-ion transport. (2) The presence of LLZTO can not only coordinate with anions, which increases the free Li^+ concentration and inhibits the movement of $DFOB^-$, but also enable Li^+ to hop from one vacancy to another on the surface region, thereby providing a fast pathway for Li^+ diffusion. Such a high t_{Li^+} is expected to reduce battery polarization by inhibiting the formation of a concentration gradient and enhancing the rate performance.

Electrochemical stability is a determining factor for electrolytes applied in highvoltage LMBs. It is demonstrated that the P(PDEM-D4)-CSE exhibits an oxidation decomposition voltage of 4.5 V, which is higher than that of the P(PDEM-D4)-PE counterpart (4.26 V; Figure S9) and previously reported PEO-based CSE [23]. The increased oxidation-resistant capability could be mainly attributed to the Lewis acid-base interactions between LLZTO and the polymer matrix, which reduce the highest occupied molecular orbitals energy levels of the polymer matrix [24–26]. Notably, all of the electrochemical properties of 5 wt% alumina-nanopowder-based CSE (CSE-5wt% Al_2O_3) are inferior to those of CSE with 5 wt% LLZTO ceramic filler (Table S7 and Figure S10) because the LLZTO ceramic filler has a higher Li-ion transference number, Li-ion conductivity, and electrochemical window than the Al_2O_3 inert filler.

3.2 Compatibility with Li metal anodes

To evaluate the compatibility with Li metal anodes, galvanostatic cycling of symmetrical Li/Li cells is conducted at a temperature of 60 °C and current densities of 0.05 mA cm^{-2} for 20 h cycling and 0.2 mA cm^{-2} (1 h in each half cycle) for 780 h cycling. As shown in Figure S11a, P(PDEM-D4)-CSE exhibits improved long-term cycling stability with a decreased polarization voltage of 0.1 V compared with the P(PDEM-D4)-PE counterpart. Reduced battery polarization can be supported by less impedance evolution of Li/Li symmetric cells with P(PDEM-D4)-CSE obtained through electrochemical impedance spectroscopy tests (Figure 2c and Table S8). These results indicate that less electrolyte decomposition occurs at the solid electrolyte interface (SEI) in the presence of P(PDEM-D4)-CSE, which is indicative of its good compatibility with Li metal electrodes. The Li plating/stripping curves of Li/Li cells at varied current densities are shown in Figure 2d. Impressively, the Li/Li cell based on P(PDEM-D4)-CSE can be steadily cycled at a current density of up to 0.6 mA cm^{-2} with low polarization voltage, indicating a favorable Li plating/stripping capability. These observations are in sharp contrast to the high polarization voltage and short-circuit behavior of the P(PDEM-D4)-PE counterpart. The noticeable polarization voltage drop at the 100th to 150th h of these electrolytes can be ascribed to the short circuit induced by dendrite growth, which is highly correlated with the nonuniform stripping/plating behavior at the Li metal surface caused by electrolyte decomposition.

Furthermore, Cu/Li cells with P(PDEM-D4)-PE or P(PDEM-D4)-CSE were assembled to investigate the Li plating/stripping behavior (Figure 2e, f, and Figure S13a, b). The corresponding Coulombic efficiencies (CEs) are presented in Figure S13c. The Cu/P(PDEM-D4)-PE/Li cell exhibits an enhanced initial CE (63.23% *vs*. 55.65%) compared with that with P(PDEM-D4)-CSE but experiences large fluctuations along with continuous overpotential increase and decreases to approximately 20% after only 154 cycles. By contrast, cells with P(PDEM-D4)-CSE deliver more stable CEs (approximately 90.2%) without any obvious deterioration detected during subsequent cycling. Furthermore, low voltage hysteresis is observed in the presence of P(PDEM-D4)-CSE (Figure 2g, and Figure S13a, b). These observations indicate that P(PDEM-D4)-CSE can induce more uniform, reversible Li plating/stripping behavior mainly because of the formation of compatible SEI. This finding is supported by the absence of mossy-like dendrites and the even surface morphology of cycled Li metal electrodes with P(PDEM-D4)-CSE (Figure 2i and Figure S14), in sharp contrast to the mossy-like dendrite morphology of the P(PDEM-D4)-PE counterpart (Figure 2h and Figure S15). Such improvement in Li plating/stripping behavior of P(PDEM-D4)-CSE could be attributed to the anion-

immobilized function of LLZTO, which can induce a uniform distribution of space charges [8].

3.3 Electrochemical performance of high-voltage $LiCoO_2$/Li batteries

To evaluate the utility of P(PDEM-D4)-CSE, 4.4-V-class $LiCoO_2$/Li-type LMBs were assembled and measured at a temperature of 60 °C and a 0.5 C rate. As shown in Figure 3a, P(PDEM-D4)-CSE has an initial capacity of 158.3 mAh g^{-1}, which is higher than that of P(PDEM-D4)-PE (154.1 mAh g^{-1}). This finding can be attributed to less electrolyte decomposition at the initial cycle in the presence of P(PDEM-D4)-CSE. Moreover, a capacity retention of 79.7%, along with an average Coulombic efficiency (ACE) of 99.74%, after 500 cycles is achieved by P(PDEM-D4)-CSE (Figure 3b). The cyclability far exceeds that of P(PDEM-D4)-PE (capacity retention of 1.6% and ACE of 99.21%; Figure 3b), indicating that P(PDEM-D4)-CSE forms a more compatible electrode/electrolyte interface. This finding is supported by reduced battery polarization with cycling (Figure S16). Notably, the rate performance of P(PDEM-D4)-CSE is superior to that of P(PDEM-D4)-PE (Figure 3c), with the discharge capacity improvement of 16% at 1 C (139.1 *vs.* 120 mAh g^{-1}; Figure 3d). Moreover, P(PDEM-D4)-CSE can regain pristine capacity at a 0.1 C rate, in stark contrast to P(PDEM-D4)-PE. Reduced battery polarization caused by electrolyte decomposition can explain this difference (Figure S17). To our knowledge, such high-voltage LMB performance is superior to most of the reported SSEs (Table S9).

To obtain a good insight into the mechanism behind the superior electrochemical performance of P(PDEM-D4)-CSE, postmortem analyses of cycled batteries were conducted. The cycled Li electrode of P(PDEM-D4)-CSE shows uniform surface morphology, in stark contrast to the rough surface of the P(PDEM-D4)-PE counterpart (Figure S18). This finding can be ascribed to the more uniform, reversible Li plating/stripping behavior of P(PDEM-D4)-CSE, which is consistent with the results of galvanostatic cycling of Cu/Li cells mentioned previously. Surface SEM imaging of cycled $LiCoO_2$ cathodes indicates that P(PDEM-D4)-CSE-based cells show good structural integrity without obvious surface cracks (Figure 4b). By contrast, some obvious intergranular

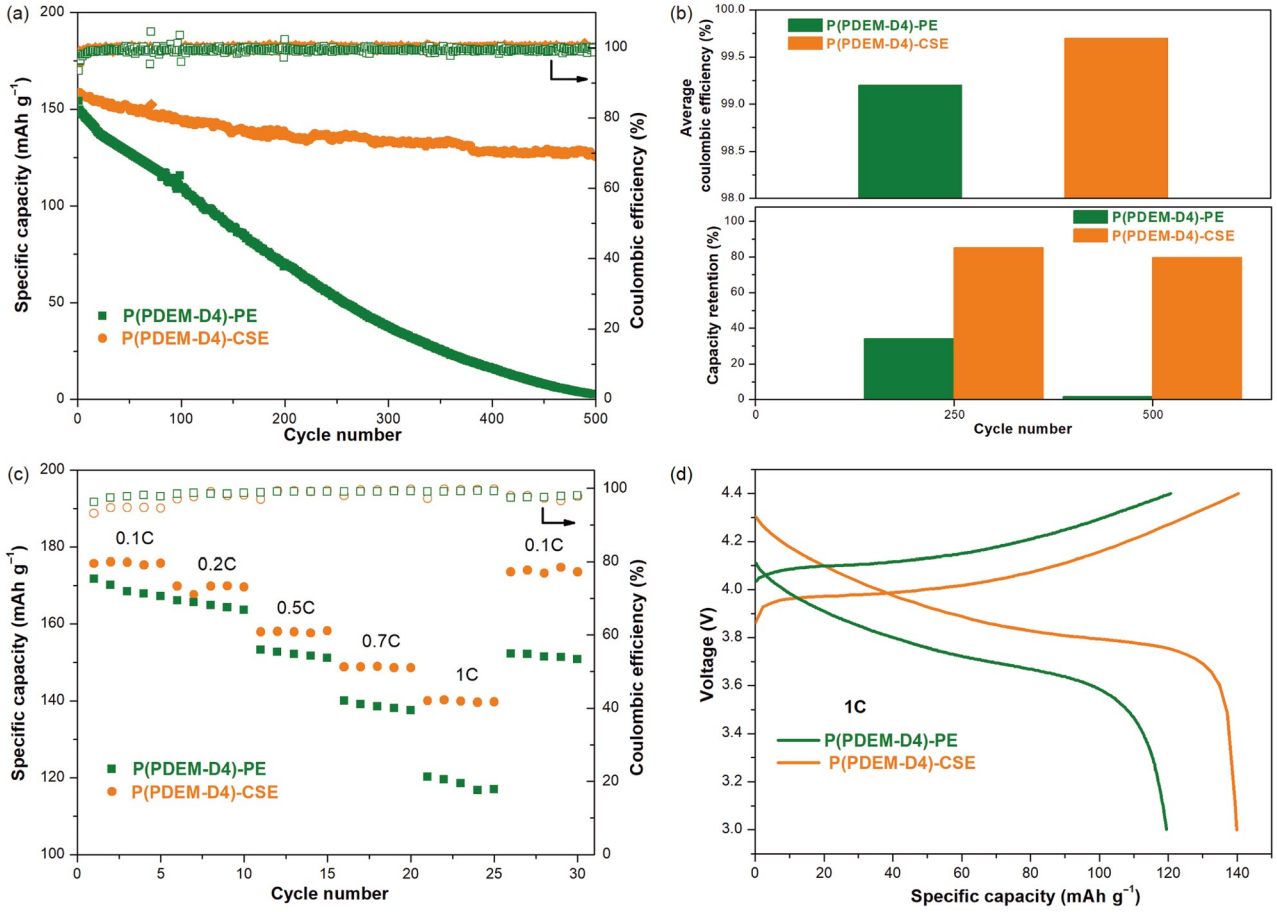

Figure 3 (a) Cycling performance of 4.4-V-class $LiCoO_2$/Li-type LMBs (3.0–4.4 V) with different electrolytes at a 0.5 C rate and a temperature of 60 °C; (b) the corresponding average Coulombic efficiency and capacity retention; (c) rate capability of 4.4-V-class $LiCoO_2$/Li-type LMBs (3.0–4.4 V) with different electrolytes; (d) the corresponding charge-discharge curves at a 1 C rate and a temperature of 60 °C (color online).

cracks are detected on the $LiCoO_2$ particles disassembled from cycled P(PDEM-D4)-PE-based cells (Figure 4a). These findings indicate less corrosion of cathode active materials in the presence of P(PDEM-D4)-CSE, which is attributed to less electrolyte decomposition. Furthermore, less electrolyte decomposition can be mirrored by the thinner CEI layer (9 *vs*. 20 nm) formed by P(PDEM-D4)-CSE (Figure 4d) than that formed by the P(PDEM-D4)-PE counterpart (Figure 4c). This observation also indicates that more compatible CEI is constructed by P(PDEM-D4)-CSE, which effectively alleviates the intergranular cracking caused by electrolyte erosion [27]. Thus, the more compatible CEI can, in part, account for the structural integrity of $LiCoO_2$ particles in cycled P(PDEM-D4)-CSE-based cells.

X-ray photoelectron spectroscopy depth profiling analysis of $LiCoO_2$ cathodes was conducted to determine how the chemical components of CEI differ in the presence of different electrolytes. As shown in Figure 4e, f, apparent enrichments in the C–O–C (286.2 eV) species on the $LiCoO_2$ cathode surface of P(PDEM-D4)-PE and P(PDEM-D4)-CSE are observed, which can be attributed to the residual polymer matrix P(PDEM-D4) that strongly adhere to the cathodes. After Ar ion sputtering to remove the polymer matrix layer, the ratio of the corresponding C–O–C peaks significantly decreases. Compared with the cycled $LiCoO_2$ cathode of P(PDEM-D4)-PE, the one close to P(PDEM-D4)-CSE shows remarkably enhanced CH_2–O–CO_2^- species at approximately 287.0 eV and Li_2CO_3/LiOH species at approximately 531.6 eV with deepening (Figure 4e, f). Notably, the CH_2–O–CO_2^- species is one of the key CEI components conducive to ion transport at the interface [28]. More Li_2CO_3/LiOH within CEI is also beneficial to the fast ion transport kinetics at the CEI layer. Moreover, enhanced LiF at 685.5 eV in the F 1*s* spectra can be observed in the

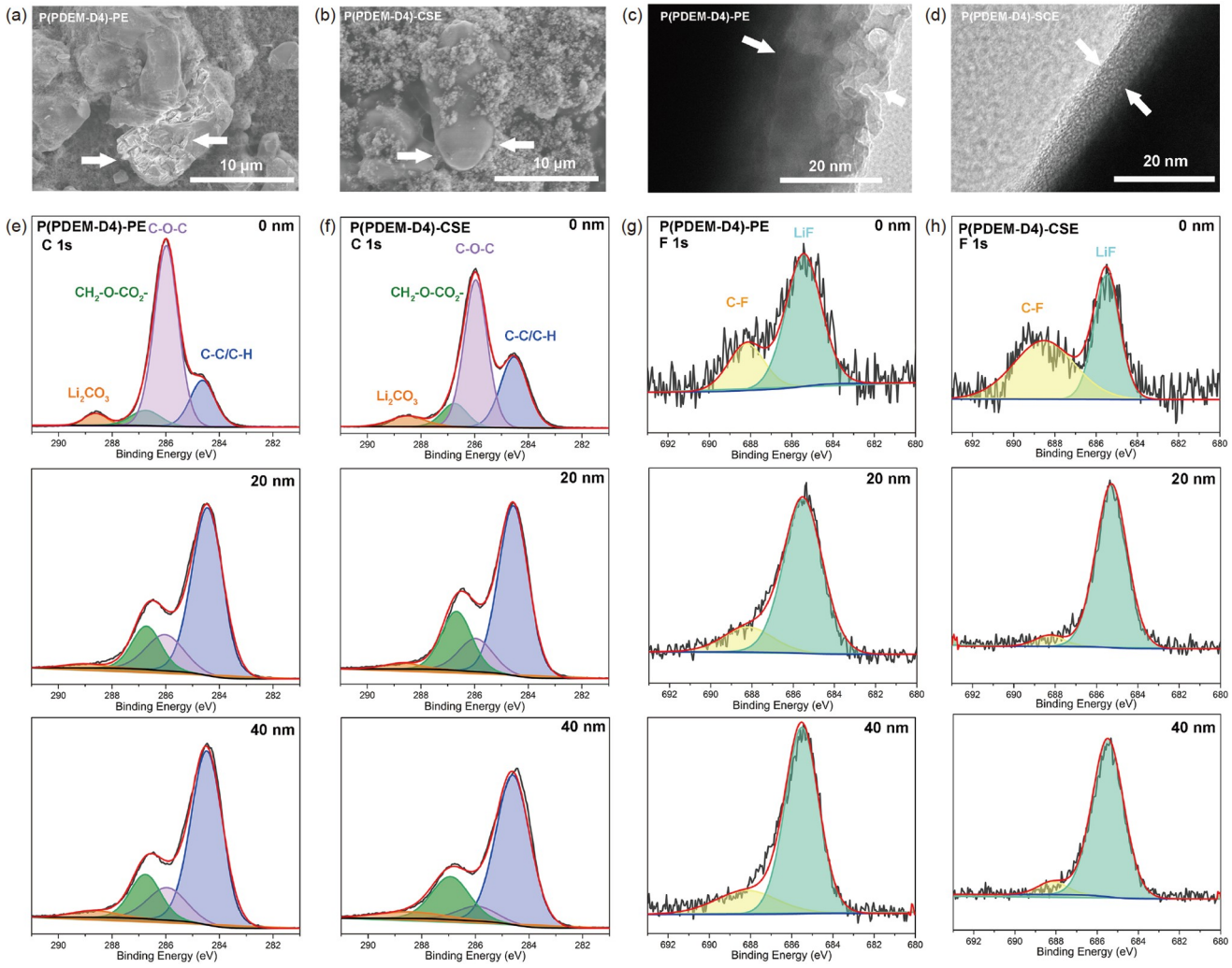

Figure 4 (a, b) Typical SEM images of the $LiCoO_2$ cathodes of P(PDEM-D4)-PE-based and P(PDEM-D4)-CSE-based Li batteries after 500 cycles; (c, d) typical transmission electron microscopy images of the $LiCoO_2$ particles of P(PDEM-D4)-PE-based and P(PDEM-D4)-CSE-based Li batteries after 500 cycles; (e–h) X-ray photoelectron spectroscopy C 1s and F 1s spectra of the $LiCoO_2$ surface of P(PDEM-D4)-PE-based and P(PDEM-D4)-CSE-based Li batteries at different etch depths after 500 cycles (color online).

inner CEI layer of P(PDEM-D4)-CSE (Figure 4g, h). Furthermore, a moderate amount of $Li_xBO_yF_z$ from the decomposition of LiDFOB is beneficial to the construction of a stable CEI (Figure S19) [29]. The aforementioned results indicate that a thin CEI layer rich in CH_2–O–CO_2^-, LiF, and Li_2CO_3/LiOH and a moderate amount of $Li_xBO_yF_z$ in P(PDEM-D4)-CSE mainly account for the superior battery performance mentioned previously.

3.4 Safety performance of high-voltage $LiCoO_2$/Li batteries

Apart from excellent battery performance, high-safety LMBs can be achieved using P(PDEM-D4)-CSE. To evaluate battery safety, a $LiCoO_2$/Li pouch battery with the as-developed CSE was fabricated and tested. Notably, the as-assembled pouch cell does not show any short-circuit behavior and can still light up a commercial red light-emitting diode lamp even after cutting several times (Figure 5a and Video S2). The superior battery safety can be further supported by the pressure measurements and accelerating rate calorimeter (ARC) tests. A pressure device with a visual pressure sensor (Figure 5b) was designed to evaluate the effect of external stress on the electrochemical performance and safety of batteries. Noting that the cell can run smoothly even at a pressure of 600 kg and only show a slight voltage fluctuation during pressure testing (Figure 5b and Video S3). ARC tests were conducted at a temperature range of 40–200 °C with a heating rate of 5 °C min^{-1} under a detected self-heating rate of 0.03 °C min^{-1} and a waiting time of 40 min. As shown in Figure 5c, no obvious self-heating behavior is observed until the temperature reaches 180 °C, which corresponds to the melting of the Li metal. Moreover, throughout the entire testing process, no obvious thermal runaway behavior (*e.g.*, swelling, fuming, or burning) was observed (the inset of Figure 5c), indicating better safety than previously reported traditional liquid-electrolyte-based LMBs that generally experience obvious thermal runaway at approximately 110 °C [30]. These results show that this CSE can achieve superior battery safety, indicating its good potential for practical application.

4 Conclusions

In summary, a novel CSE comprising a star-shaped siloxane-based polymer electrolyte and LLZTO ceramic filler has been prepared for high-voltage LMBs *via* an *in situ* preparation approach, which endows it with close interface contact in LMBs. Compared with P(PDEM-D4)-PE, the existence of the LLZTO ceramic filler helps achieve faster ion transport, extended electrochemical stability windows (0–4.5 *vs.* 0–4.26 V), and enhanced t_{Li^+} (0.53 *vs.* 0.39), which could be mainly attributed to the Lewis acid-base interactions, such as $DFOB^-$/polymer skeleton and $DFOB^-$/surface of nanosized LLZTO. Moreover, the as-developed CSE can achieve homogeneous Li deposition. As a result, P(PDEM-D4)-CSE enables the 4.4 V $LiCoO_2$/Li battery to exhibit excellent cycling stability and rate performance at a temperature of 60 °C. The mechanism behind such superior

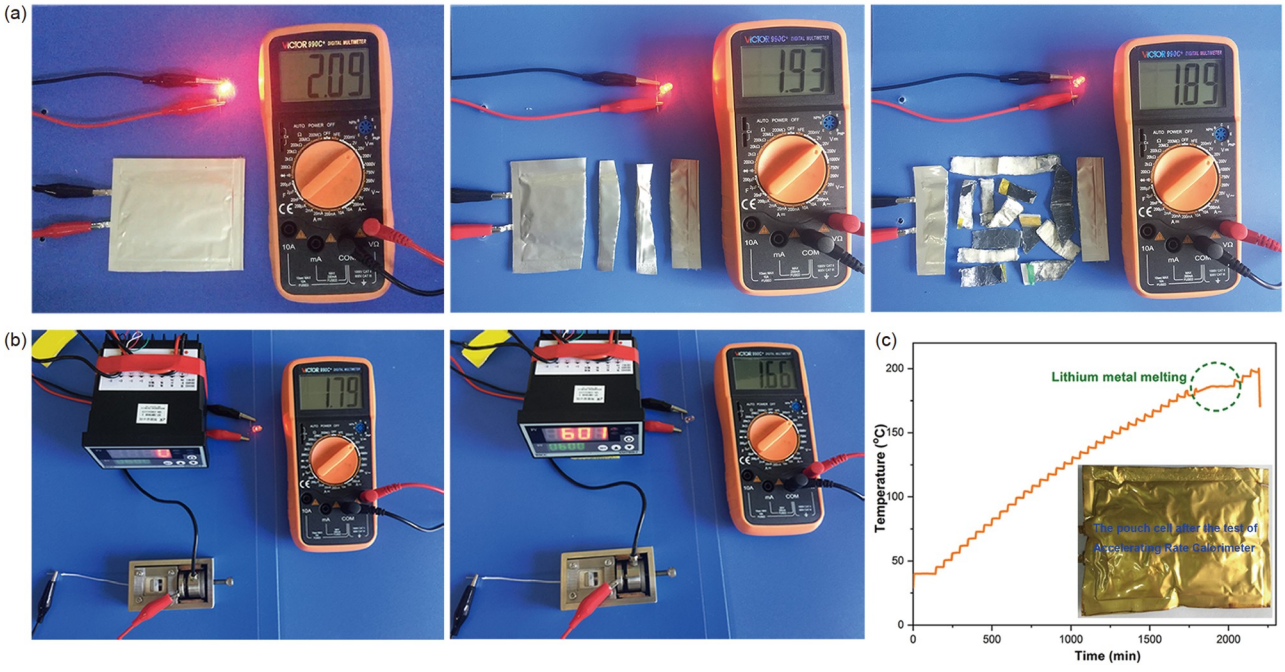

Figure 5 (a) Cutting test, (b) pressure simulation experiment, and (c) ARC test of $LiCoO_2$/Li pouch batteries with the as-developed CSE at fully charged state. The inset of (c) is the corresponding pouch cell after the ARC test (color online).

electrochemical performance is the formation of a compatible electrode/electrolyte interface, as evidenced by the postmortem analysis of cycled LMBs. To our knowledge, such high-voltage solid-state LMBs are scarcely reported in previous work. Remarkably, all-solid-state pouch cells with P(PDEM-D4)-CSE also exhibit outstanding safety characteristics under harsh conditions. This work provides an important guide for the rational design of SSEs for high-voltage LMBs.

Acknowledgements This work was supported by the Strategic Priority Research Program of the Chinese Academy of Sciences (XDA21070304), the National Natural Science Foundation of China (51502319, 51803230, 52003285, 21901248), the Natural Science Foundation of Shandong Province (ZR2021QE039, ZR2021QE149, ZR2020MB082), the Key Scientific and Technological Innovation Project of Shandong (2020CXGC010401), and the Taishan Scholars of Shandong Province (ts201511063).

Conflict of interest The authors declare no conflict of interest.

Supporting information The supporting information is available online at http://chem.scichina.com and http://link.springer.com/journal/11426. The supporting materials are published as submitted, without typesetting or editing. The responsibility for scientific accuracy and content remains entirely with the authors.

1 Jiao S, Ren X, Cao R, Engelhard MH, Liu Y, Hu D, Mei D, Zheng J, Zhao W, Li Q, Liu N, Adams BD, Ma C, Liu J, Zhang JG, Xu W. *Nat Energy*, 2018, 3: 739–746
2 Zhao CZ, Duan H, Huang JQ, Zhang J, Zhang Q, Guo YG, Wan LJ. *Sci China Chem*, 2019, 62: 1286–1299
3 Xiao Y, Xu R, Yan C, Liang Y, Ding JF, Huang JQ. *Sci Bull*, 2020, 65: 909–916
4 Lv Z, Zhou Q, Zhang S, Dong S, Wang Q, Huang L, Chen K, Cui G. *Energy Storage Mater*, 2021, 37: 215–223
5 Han X, Gong Y, Fu KK, He X, Hitz GT, Dai J, Pearse A, Liu B, Wang H, Rubloff G, Mo Y, Thangadurai V, Wachsman ED, Hu L. *Nat Mater*, 2017, 16: 572–579
6 Zeng XX, Yin YX, Li NW, Du WC, Guo YG, Wan LJ. *J Am Chem Soc*, 2016, 138: 15825–15828
7 Tan SJ, Zeng XX, Ma Q, Wu XW, Guo YG. *Electrochem Energy Rev*, 2018, 1: 113–138
8 Zhao CZ, Zhang XQ, Cheng XB, Zhang R, Xu R, Chen PY, Peng HJ, Huang JQ, Zhang Q. *Proc Natl Acad Sci USA*, 2017, 114: 11069–11074
9 Huo H, Chen Y, Luo J, Yang X, Guo X, Sun X. *Adv Energy Mater*, 2019, 9: 1804004
10 Bae J, Li Y, Zhang J, Zhou X, Zhao F, Shi Y, Goodenough JB, Yu G. *Angew Chem Int Ed*, 2018, 57: 2096–2100
11 Huo H, Zhao N, Sun J, Du F, Li Y, Guo X. *J Power Sources*, 2017, 372: 1–7
12 Wang Q, Zhang H, Cui Z, Zhou Q, Shangguan X, Tian S, Zhou X, Cui G. *Energy Storage Mater*, 2019, 23: 466–490
13 Dong Z, Wei J, Yue H, Zhang K, Wang L, Li X, Zhang Z, Yang W, Yang S. *J Colloid Interface Sci*, 2021, 595: 35–42
14 Xue Z, He D, Xie X. *J Mater Chem A*, 2015, 3: 19218–19253
15 Zhou D, He YB, Liu R, Liu M, Du H, Li B, Cai Q, Yang QH, Kang F. *Adv Energy Mater*, 2015, 5: 1500353
16 Zhou D, Tkacheva A, Tang X, Sun B, Shanmukaraj D, Li P, Zhang F, Armand M, Wang G. *Angew Chem Int Ed*, 2019, 58: 6001–6006
17 Zhao Q, Liu X, Stalin S, Khan K, Archer LA. *Nat Energy*, 2019, 4: 365–373
18 Wang Y, Ju J, Dong S, Yan Y, Jiang F, Cui L, Wang Q, Han X, Cui G. *Adv Funct Mater*, 2021, 31: 2101523
19 Yan Y, Ju J, Dong S, Wang Y, Huang L, Cui L, Jiang F, Wang Q, Zhang Y, Cui G. *Adv Sci*, 2021, 8: 2003887
20 Quartarone E, Mustarelli P. *Chem Soc Rev*, 2011, 40: 2525–2540
21 Aldalur I, Martinez-Ibañez M, Piszcz M, Rodriguez-Martinez LM, Zhang H, Armand M. *J Power Sources*, 2018, 383: 144–149
22 Liu W, Liu N, Sun J, Hsu PC, Li Y, Lee HW, Cui Y. *Nano Lett*, 2015, 15: 2740–2745
23 Zhang J, Zhao N, Zhang M, Li Y, Chu PK, Guo X, Di Z, Wang X, Li H. *Nano Energy*, 2016, 28: 447–454
24 Zhou Q, Ma J, Dong S, Li X, Cui G. *Adv Mater*, 2019, 31: 1902029
25 Park C, Kim DW, Prakash J, Sun YK. *Solid State Ion*, 2003, 159: 111–119
26 Liu W, Lin D, Sun J, Zhou G, Cui Y. *ACS Nano*, 2016, 10: 11407–11413
27 Han JG, Lee JB, Cha A, Lee TK, Cho W, Chae S, Kang SJ, Kwak SK, Cho J, Hong SY, Choi NS. *Energy Environ Sci*, 2018, 11: 1552–1562
28 Eshetu GG, Diemant T, Grugeon S, Behm RJ, Laruelle S, Armand M, Passerini S. *ACS Appl Mater Interfaces*, 2016, 8: 16087–16100
29 Liang JY, Zhang XD, Zeng XX, Yan M, Yin YX, Xin S, Wang WP, Wu XW, Shi JL, Wan LJ, Guo YG. *Angew Chem Int Ed*, 2020, 59: 6585–6589
30 Feng X, Ren D, He X, Ouyang M. *Joule*, 2020, 4: 743–770